metals

MDPI

Article

Microtexture and Rolling Deformation Behavior Analysis of the Formation Mechanism Fe_3O_4 at the Interface Formed on Hot-Rolled High-Strength Steel

Chao Wang, Huibin Wu *, Zhichao Li, Pengcheng Zhang and Leilei Li

Collaborative Innovation Center of Steel Technology, University of Science and Technology Beijing, Beijing 100083, China; B20170496@xs.ustb.edu.cn (C.W.); lizhichao1225@163.com (Z.L.); zhangpengcheng@ustb.edu.cn (P.Z.); b20200555@xs.ustb.edu.cn (L.L.)

* Correspondence: whbustb@163.com; Tel.: +86-1391-029-7962

Abstract: In order to better understand the formation mechanism of tertiary oxide scale in high-strength steel during hot rolling, the microtexture of the oxide layer has been characterized and analyzed by the electron backscatter diffraction (EBSD) method. The results show that the Fe_3O_4 phase in the oxide layer has a two-phase heterogeneous morphology, Fe_3O_4 in the oxide layer comprises columnar grains, and Fe_3O_4 near the substrate comprises spherical grains. As the reduction rate increases, the Fe_2O_3 layer is gradually wedged into the surface of the Fe_3O_4 layer. Fe_3O_4 forms a <110> fiber texture at a reduction rate of 10%. The inner layer of the oxide scale comprises spherical grains, and Fe_3O_4 is preferentially nucleated and precipitated in the direction of Fe surface grains <110> texture. With the increase in the reduction rate, the {112}<−1−21> directional slip system shows the lowest Schmidt factor value, so the grains with a low Schmidt factor exhibit higher stored strain energy. The formation of the spherical Fe_3O_4 seam layer close to the steel matrix is the result of the combined effect of the stress state at the matrix and ion diffusion.

Keywords: oxide scales; grain orientation; texture; EBSD

check for updates

Citation: Wang, C.; Wu, H.; Li, Z.; Zhang, P.; Li, L. Microtexture and Rolling Deformation Behavior Analysis of the Formation Mechanism Fe_3O_4 at the Interface Formed on Hot-Rolled High-Strength Steel. *Metals* **2021**, *11*, 312. https://doi.org/10.3390/met11020312

Received: 11 January 2021
Accepted: 8 February 2021
Published: 10 February 2021

Publisher's Note: MDPI stays neutral with regard to jurisdictional claims in published maps and institutional affiliations.

Copyright: © 2021 by the authors. Licensee MDPI, Basel, Switzerland. This article is an open access article distributed under the terms and conditions of the Creative Commons Attribution (CC BY) license (https://creativecommons.org/licenses/by/4.0/).

1. Introduction

Since hot-rolled steel sheets are always produced in high-temperature environments, oxide scale is always accompanied by the entire process, and it is inevitably formed on the surface of the steel. Proper control is related to the surface quality of the final product [1,2]. Before subsequent processing such as cold rolling, the steel plate needs to be pickled to remove the scale. On the other hand, before application, it is possible to maintain tight scale formation on the steel plate without pickling. Therefore, it is very important to understand the origin of pickling-free steel, which is closely related to the deformation behavior of the oxide scale on the surface of the hot-rolled steel. Two oxide sub-layers are usually formed on the surface of iron-based materials when the temperature is lower than 570 °C, and three oxide layers are formed when the temperature is higher than 570 °C [3]. The two different oxides have different formation mechanisms and properties [4]. When the temperature is above 650 °C, the main content of the oxide scale is wustite; on the contrary, the main phase of oxide scale is magnetite when the temperature is low. Fe_2O_3 is distributed on the surface of the oxide layer and the content is low [5–7].

The phase transition of FeO and the precipitation behavior of magnetite at high temperatures play a crucial role in the ratio of the three phases of oxide scale. These transformation behaviors are closely related to the precipitation of alloying elements in the steel, the rolling process, and the heat treatment process. The electron backscatter diffraction (EBSD) method has been used to research the composition and phase distribution of the oxide scale, but there are few studies on the microstructure and interface properties. Normally, the oxide layer is composed of Fe_2O_3, Fe_3O_4, and FeO, although the Fe_2O_3

content on the surface is low. In particular, due to the thin Fe_2O_3 layer or the fact that it is polished off during sample preparation, EBSD detection is more difficult [8]. In addition to phase identification, the microstructure and orientation relationship of the oxide phase is still being investigated. Therefore, the high-temperature oxidation mechanism of high-strength steel is considered to be related to the high-temperature oxidation behavior [9], stress condition, and the subsequent preferred orientation of oxide scale [10,11]. In the undeformed oxide layer, due to the defect structure of the oxide scale, there may also be a cubic crystal system orientation relationship between the FeO and Fe_3O_4 [12]. It mainly relies on the data of macro-texture, rather than micro-texture, and rarely considers the influence of fine micro-texture on the formation of Fe_3O_4 seam layer.

Extensive research has been conducted on the formation of the oxide layer, but there are very few reports on the deformation behavior of the oxide scale during hot rolling [13,14]. On the contrary, the thermal simulation gleeble plane strain compression is mainly used to study the deformation behavior of the oxide layer. This research method does not consider the influence of the steel/roll contact on the oxide scale during the hot rolling process because there is a temperature gradient between them, and the studied oxide scale is a non-contact surface. So far, the research on FeO decomposition caused by magnetite precipitation is limited to isothermal transformation behavior [15,16]. Little is known about the effect of preferential grain growth in the magnetite layer. Therefore, it is necessary to analyze the phase transition behavior of the deformed oxide layer and the bonding force of the matrix, as well as the microstructure changes and microtexture evolution caused by the rolling–cooling coupling process.

In this study, the method of combining EBSD analysis with mechanical and argon ion polishing sample preparation was used to characterize the microtexture of the oxide layer after different reduction rates and cooling. The influence of the grain morphology and texture orientation at the interface on the phase transition of Fe_3O_4 is obtained, and the oxide layer structure of pickling-free steel is obtained through rolling and subsequent cooling.

2. Materials and Methods

The sample used was high-strength steel, and the content of the alloying element is shown in Table 1.

Table 1. Compositions and concentration (wt.%) of the steel.

Fe	C	Si	Cr	Mn	P	Al
Balance	0.06	0.21	0.36	1.48	0.008	0.03

The samples with a size of 300 × 80 × 8 mm^3 were cut from the high-strength steels. Before rolling, SiC paper with 2000 mesh was used to grind the surface of all samples to the same surface finish and cleaned in an acetone solution. Finally, it was ensured that the samples before the oxidation experiment had the same surface state. X-ray diffraction with Cu Kα radiation (λ = 1.54 Å) was used to identify the phases in the oxide scale. The voltage was 45 KV, the current was 180 mA, and the diffraction angle (2θ) was from 10° to 90°. A combination of Raman and X-ray diffraction (XRD) was performed in order to determine the crystalline phases of the oxide scales.

The hot rolling test was carried out in the 4-roller experimental rolling mill combined with a laminar cooling system. Among them, the rapid cooling of the steel was realized by controlling the nozzle opening degree and the roller speed of the roller table, and the polished sample was heated to the austenitizing temperature for subsequent rolling. The following process was performed for each oxidation test. The sample was placed in the heating furnace, and then the sample was heated to the austenitizing temperature (920 °C) under argon protection and kept for 20 min to ensure that the horizontal and vertical temperature of the sample is consistent. The rolled sample was cooled to the coiling temperature by a laminar flow cooling system and then cooled to room temperature in an

air atmosphere, thereby obtaining a tertiary oxide scale. The hot rolling process of the steel sheets is shown in Figure 1.

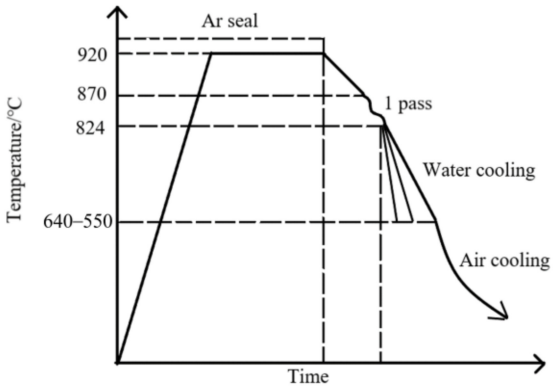


Figure 1. The heat treatment and rolling experiment process.

Each steel plate was heated to a single austenitizing temperature of 920 °C, and then at different cooling rates to obtain the structure; the room temperature structure was ferrite and pearlite phase. The cooling rates were 11, 18, 27 °C/s, and the reduction rates were set to 10%, 15%, and 27%. Table 2 shows the rolling process and experimental parameters.

Table 2. Hot rolling experimental parameters for oxidation tests.

Parameters	1	2	3
Reheating time, min	20	20	20
Furnace temperature, °C	920	920	920
Rolling reduction, %	10	15	27
Cooling rate, °C/s	11	18	27

After the sample is mounted, it was polished with 2000 mesh SiC sandpaper until the surface was smooth and clean, then polished with diamond abrasive paste; finally, a 4% nitric acid alcohol solution was used to corrode the cross-section of the sample, and then rinsed and dried with water and alcohol for scanning electron microscope observation. EBSD samples were cut from the central area of the steel surface along the rolling direction and polished with 2000 mesh SiC sandpapers (their cross-sections were inlaid with a conductive insert powder). As the oxide phase and the steel matrix possess different materials, traditional polishing technologies could not be used for EBSD sample preparation. Hence, a vibration polishing machine was used to accurately polish the oxide scale. The grinding time was not less than 120 min, and a SiO_2 suspension was used as the lubricant. Moreover, the speed of the turntable was controlled at below 350 r/min to ensure a better suspension concentration around the oxide layer to remove the stress layer. The sample after vibration polishing was finely polished with an argon ion polishing equipment. The voltage of the ion beam system was selected to be 5KV, and the ion grinding time was not less than 3 h. The microstructural characterization of the oxide layer was performed by a scanning electron microscope equipped with an EBSD probe (Oxford) at an accelerating voltage of 20 kV (working distance = 15 mm and scanning step length = 0.06 μm). The normal direction (ND) is defined as perpendicular to the surface of the sample, which is the direction of scale growth, and the length direction of the sample was defined as the rolling direction (RD) of the hot-rolled steel sheet. The microstructure analysis was performed on a field emission scanning electron microscope (SEM), and an EBSD detector for analyzing the microtexture was installed. Each phase of the oxide scale had a different space group. The steel matrix was Im-3m, FeO was Fm-3m, Fe_3O_4 was Fd-3m, and Fe_2O_3 was R-3c. At the same time, $\theta \geq 15^\circ$ are defined as high-angle grain boundaries (HAGBs), and $2^\circ \leq \theta < 15^\circ$ are

low-angle grain boundaries (LAGBs). The phase choices are Fe phase, wustite, magnetite, and hematite.

3. Results and Discussion

3.1. Characteristics of the Steel Matrix

The properties of the high-strength steel matrix were investigated prior to the rolling experiment. Figure 2a,b display the SEM and EBSD images of the high-strength steel substrate. The microstructure of the steel matrix was composed of ferrite and pearlite (the volume fractions of ferrite and pearlite accounted for 90% and 10%, respectively). As the proportion of α-Fe in the steel matrix was much higher than the content of pearlite, only the α-Fe phase was selected for the steel matrix in the EBSD analysis.

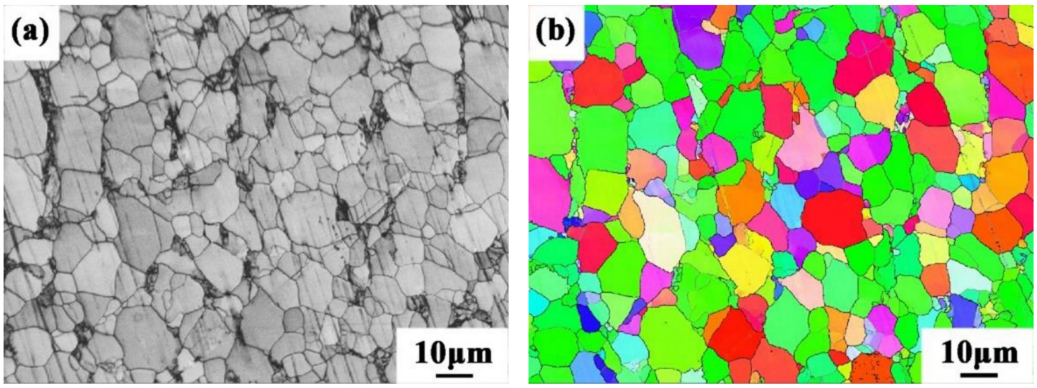


Figure 2. (**a**) Surface morphology and (**b**) electron backscatter diffraction (EBSD) image of the high-strength steel substrate.

Figure 3 is a schematic diagram of the EBSD grain boundary evolution of experimental steel under different process conditions. Low-angle grain boundaries ($2^\circ \leq \theta < 15^\circ$) are shown in black, and high-angle grain boundaries ($\theta \geq 15^\circ$) are shown in blue. At the same time, the size changes of grains under different reduction rates are quantified. When the reduction rate increases from 10% to 27%, the matrix grains are elongated, and the number of sub-grains increases. As the reduction rate increases, the increase of flat grains in the steel matrix will have a corresponding effect on the oxide layer formed on the surface.

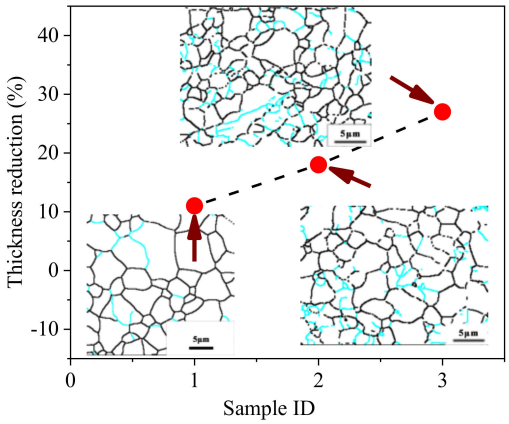


Figure 3. Distribution map of backscattered diffraction grain boundary of high-strength steel matrix at different reduction rates and cooling rates after hot rolling. The low-angle grain boundaries (2–15°) are in black and high angle boundaries (>15°) are shown in blue based on the misorientation angle.

3.2. Microstructure of Oxide Layers

The surface oxide layer of the steel is composed of wustite, hematite, magnetite, and ferrite. Figure 4 shows the electron backscatter diffraction pattern of the oxide scale at different reduction rates and cooling rates after the samples were heated at 920 °C and then cooled to 870 °C. Among them, blue, red, pink, and green represent ferrite, hematite, magnetite, and wustite, respectively. The oxide layer is composed of the outermost massive hematite layer, the central columnar Fe_3O_4 layer, and the spherical fine-crystalline magnetite layer, especially the joints of small spherical particles near the matrix (also named "magnetite seam layer"). It was found that Fe_2O_3 grains gradually wedged into the deformed magnetite surface when the rolling reduction rate was low (Figure 4a). This is different from the previous research results obtained by using a thermal simulation test machine for compression deformation in that when the cold roll was compressed to the hot samples, there was a temperature gradient, which may have led to the outermost phase of the oxide layer, namely hematite.

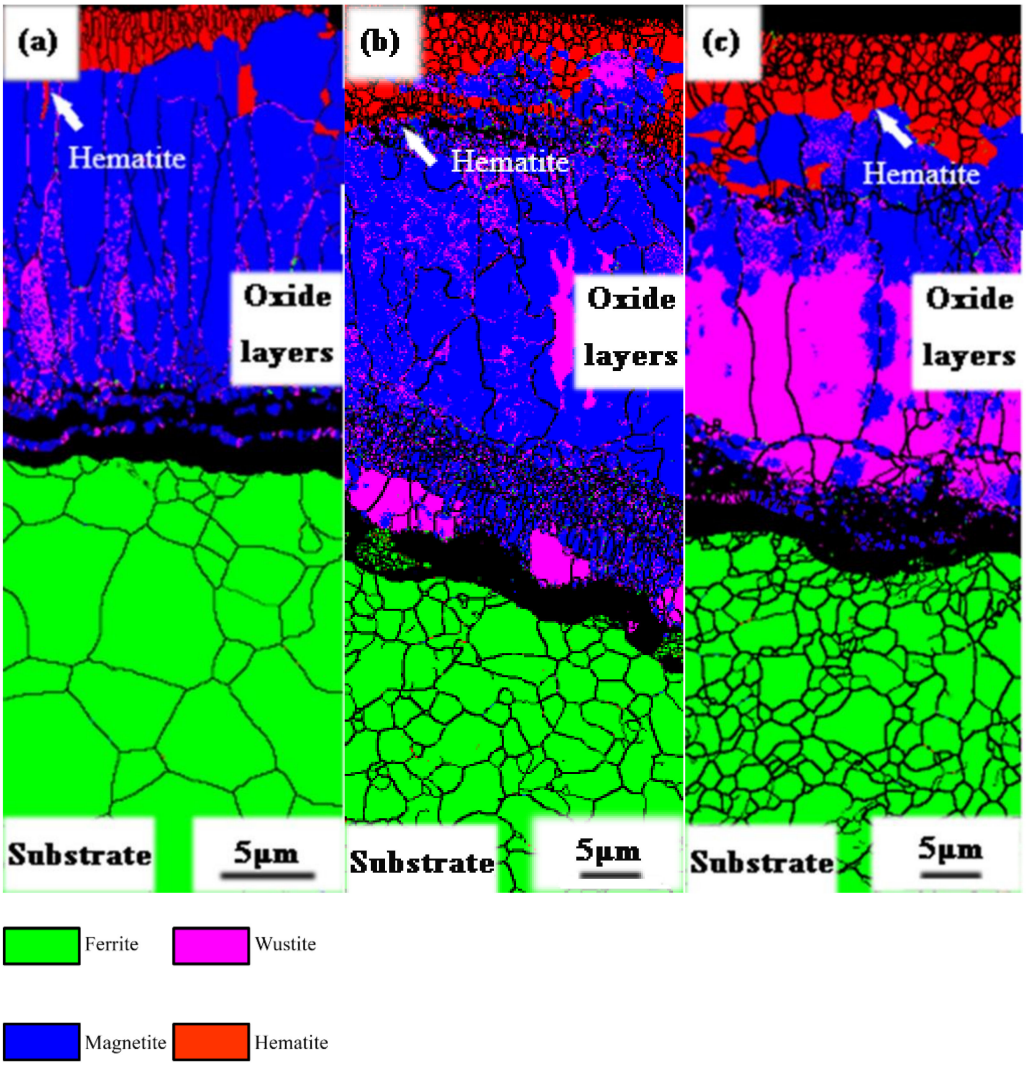


Figure 4. EBSD phase maps of the high strengh steel reheated at 920 °C, cooled to 870 °C, with the reduction rate and cooling rates of (**a**) 10 %, 11 °C/s, (**b**) 15%, 18 °C/s, and (**c**) 27 %, 27 °C/s.

Since the spinel oxide usually formed inside the substrate is not a simple iron oxide compound but a mixed oxide containing elements such as Si or Cr, the interface point scan is performed by a Raman spectrometer (Figure 5). It can be determined by the Raman peak that this spinel oxide is mainly Fe-Cr and Fe-Si spinel compounds. XRD analysis

also shows that the main structure of the oxide layer is Fe_2O_3 on the surface, Fe_3O_4 in the middle layer, Fe_2SiO_4, and $FeCr_2O_4$ compounds at the interface.

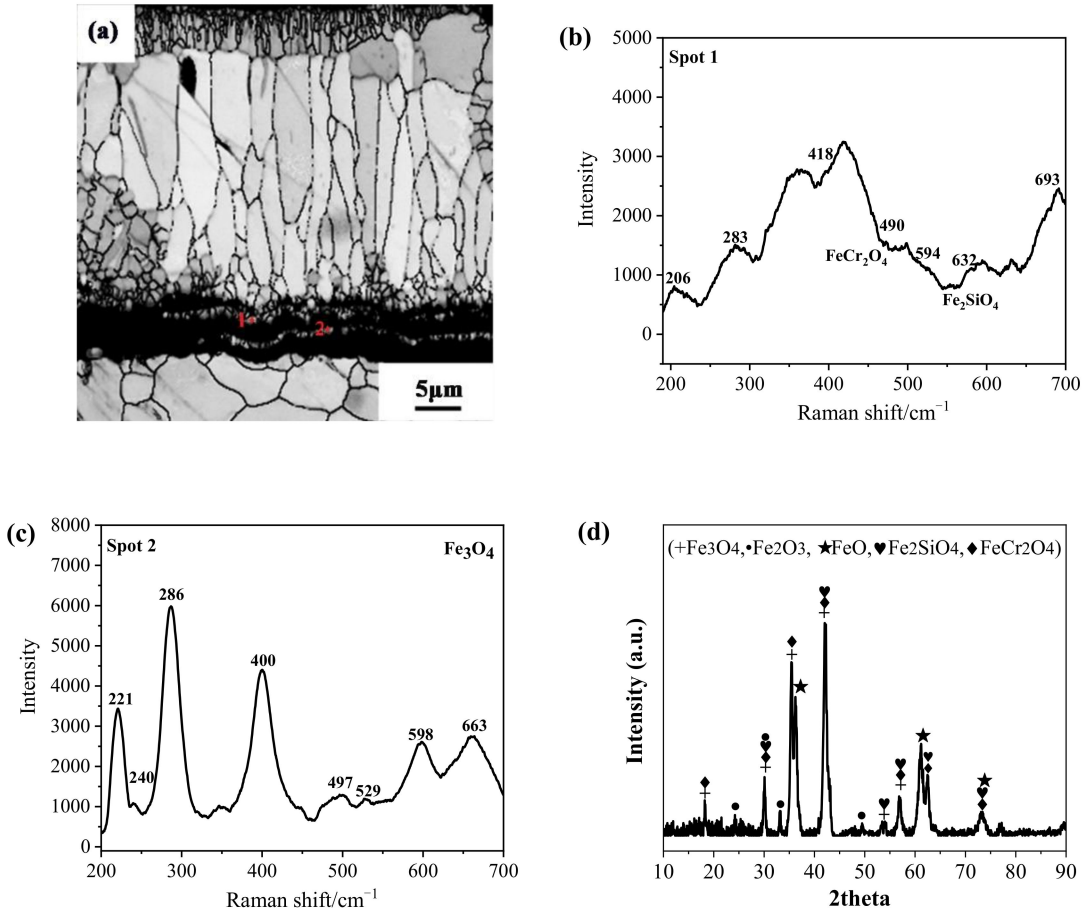


Figure 5. Raman spectroscopy spot analysis of the oxide scale with the thickness reduction of 10% and cooling rate of 11 °C/s, (**a**) oxide layer morphology and position, (**b**,**c**) Raman spectrum at the interface of the oxide scale and the substrate. (**d**) XRD spectra of the oxide layers.

The results of Raman spectroscopy and EBSD show that the fine grains at the interface are a Fe_3O_4 phase. Therefore, it presents the microstructure of a dual magnetite layer, the outer layer presents a columnar crystal structure, and the Fe_3O_4 grains at the interface are more refined and tend to be equiaxed. It is generally believed that the influence of the magnetite layer on the growth rate is relatively small, but the growth mode of the magnetite layer at the interface is very different from that of the oxide layer. Previous investigations have shown that different alloying element compositions have an important influence on the growth of scale on the surface of high-strength steel. In particular, adding only 0.1 wt% of Si element to steel is enough to make the Fe_3O_4 layer grow in a dual structure at 500 °C. The microstructure of the steel matrix has an important influence on the appearance of dual structures, especially for slow-growing oxides such as magnetite, which can hardly be found in FeO and Fe_2O_3. However, its influence on the formation of the columnar magnetite layer is unclear. In addition, as shown in Figure 6, residual fine-grained FeO oxide is distributed on the grain boundaries of magnetite. At the same time, as the reduction rate increases, the surface layer of hematite gradually wedges into the cracks inside the oxide layer.

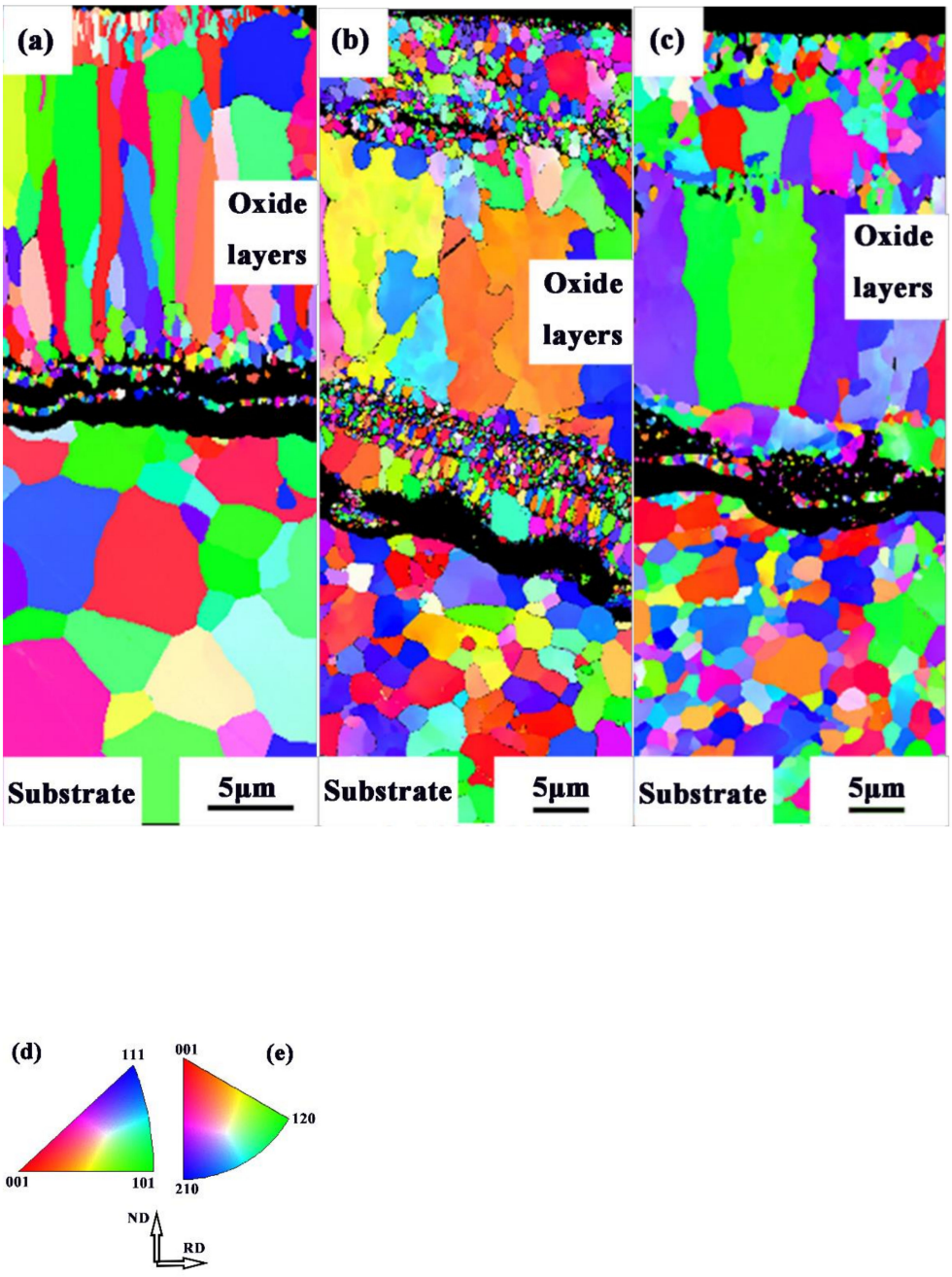


Figure 6. Electron backscatter diffraction grain orientation distribution map with the reduction rate and cooling rates of (**a**) 10%, 11 °C/s, (**b**) 15%, 18 °C/s, and (**c**) 27%, 27 °C/s, a color distinction for the (**d**) cubic crystal system, FeO, and Fe_3O_4, (**e**) Fe_2O_3.

3.3. The Characterization of Deformed Oxide Scales

Figure 6 shows the distribution of the grain orientation of the oxide scale measured by electron backscatter diffraction (IPF graph). As the rolling reduction rate and cooling rate increased, the microstructure of the oxide layer was constantly changing. Figure 6d shows the coding rules for the cubic crystal system of FeO, Fe_3O_4, and α-Fe. Correspondingly, Figure 6e shows the case of the triangular crystal system α-Fe. From the grain orientation distribution map of the oxide layer, it can be found that the microstructure of the double-layer Fe_3O_4 in the oxide scale is different. The outer layer of the oxide scale has a columnar crystal structure, while the inner layer of Fe_3O_4 has more refined grains, and the shape is isometric. The IPF diagram of the grain orientation of the oxide scale Fe_3O_4 intermediate

layer shows that the crystal grains are columnar microstructures, and the interface is the Fe_3O_4 seam layer. This two-phase heterogeneous structure is under high-temperature oxidation conditions, and the oxide scale grains grow laterally. The resulting residual FeO is transformed into Fe_3O_4 with a columnar structure.

Previous studies have shown that at high temperatures, the particle-shaped FeO is elongated along the oxide/steel interface, and after cations and electrons diffuse, they remain intact at the interface. Therefore, for high-strength steel, when the temperature is higher than 570 °C, the FeO eutectoid decomposes into columnar Fe_3O_4 in the oxide layer. As shown in Figure 6, however, at a lower reduction rate and cooling rate, the texture of Fe_3O_4 lacks a strong peak, which means that the controlled rolling and controlled cooling process not only affects the grain size of the steel matrix but also has an important influence on the texture orientation distribution of the oxide scale.

Figure 7 shows the distribution of grain boundary misorientation of the oxide layer. The selected oxide scale sample has a rolling reduction rate of 15% and a cooling rate of 18 °C/s. It can be seen from the grain boundary misorientation distribution graph that Fe_3O_4, which is dominated by a cubic crystal system, has its first largest peak at 53.5° and a cutoff point at an orientation angle of 62.5°.

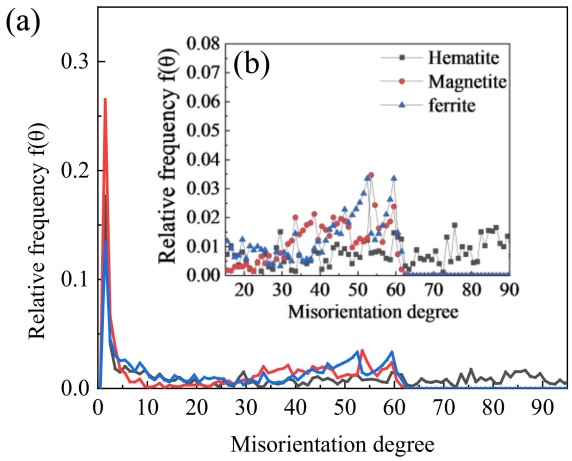


Figure 7. Distribution map of grain boundary misorientation of different phases in the oxide scale, the sample with the reduction rate of 15% and cooling rate of 18 °C/s, (**a**) all boundaries. (**b**) high angle grain boundaries with misorientation >15°.

For the triangular crystal system α-Fe_2O_3, it can be seen from the figure that there are obvious peak changes at 31°, 64°, and 73°, although the high-intensity peaks of α-Fe and α-Fe_2O_3 are at 55° and 60° orientations. The difference returns to the low peak, but the high-density small-angle grain boundary appears in Figure 7b. Generally, for polycrystalline metal materials, the appearance of low-angle grain boundaries can provide barriers to the propagation of cracks, that is to say, the low-angle grain boundaries minimize the solute effect, and the interaction between the grain boundary interface and the fissile dislocation is also reduced [17].

It can be concluded that these low-angle grain boundaries of α-Fe_2O_3 can effectively improve the surface quality defects of the oxide scale caused by the mismatch of the Fe_3O_4 lattice. In addition, under different reduction rates and cooling rates, the grain size of each phase is generally less than 4.5 μm, as shown in Figure 8a,b. Although there are some abnormal grains with a grain size larger than 4.5 μm, FeO and Fe_3O_4 have similar grain size distribution with a steel matrix, while α-Fe_2O_3 has a larger grain size when the reduction rate is low (Figure 8b). It can be inferred that α-Fe_2O_3 alternately grows into the cracks. Indeed, hematite grains gradually wedge into the surface of magnetite in the deformed oxide scale at a lower thickness reduction. This suggests that the oxygen diffusion is facilitated due to the cracking within the thin outer-layered magnetite, and therewith

magnetite is further oxidized to hematite. The higher thickness reduction of 27% tends to result in at least 80% density for porosity in contrast with the former two thickness reductions of 10% and 15%. This is because the strain can now be relieved by substrate yield, so there will be little scale cracking, and corresponding hematite remains on the outer layer.

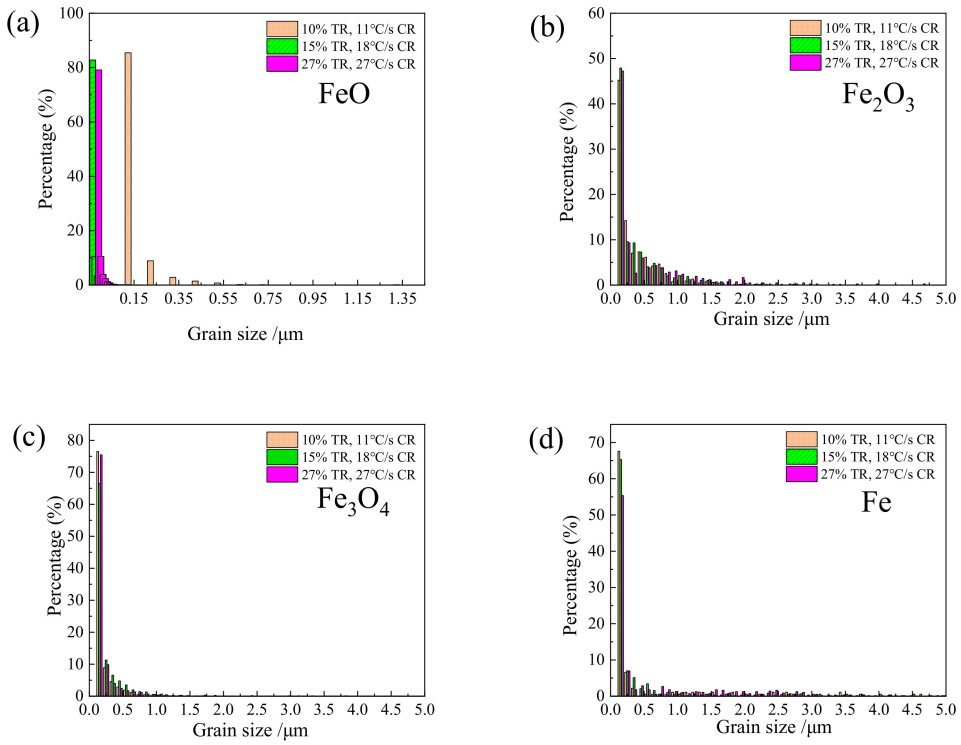


Figure 8. Histogram of oxide phase grain size distribution for (**a**) FeO, (**b**)Fe2O3, (**c**) Fe3O4, (**d**) Fe and the steel with the thickness reduction of 10%, 15%, and 27%, and a cooling rate of 11, 18, 27 °C/s.

3.4. Microtexture Evolution Process of Deformed Oxide Layer

The pole figures of FeO, Fe_3O_4, Fe, and Fe_2O_3 obtained under different processes are shown in Figures 9–11. When Fe_3O_4 reduction rate is 10% and cooling speed is 11 °C/s, from Figure 9a, it can be concluded that Fe_3O_4 rormeda {114} fiber texture component, and with the increase of the reduction rate, Fe_3O_4 gradually formed a stronger {112} fiber texture on the surface of the oxide layer (Figure 11b). Its intensity was f(g) = 18.51. This change in texture type confirms that polycrystalline materials require longer oxidation time than iron single crystals [18].

It can be found in Figures 9, 10 and 11c that the crystallographic texture of the steel matrix is weak, mainly manifested as a shear component. This type of texture often appears when rolling the surface area of the steel in the past, and it also appears in the dynamic transformation process of deformed austenite under different cooling conditions [19].

Figures 9, 10 and 11d show the evolution process of α-Fe_2O_3 texture in the oxide scale as the reduction rate and cooling rate increases. It can be seen that when the reduction rate is 10% and the cooling rate is 11 °C/s, α-Fe_2O_3 has a mixed-orientation component of {−12−10}<10−10> and {01−10}<2−1−10> texture (Figure 9d), with density strength f(g) = 7.26. It can be concluded that the reduction increases to 27% (Figure 11d) and α-Fe_2O_3 has a fiber texture component close to {0001}<2−1−10> while retaining {01−10}<2−1−10> texture.

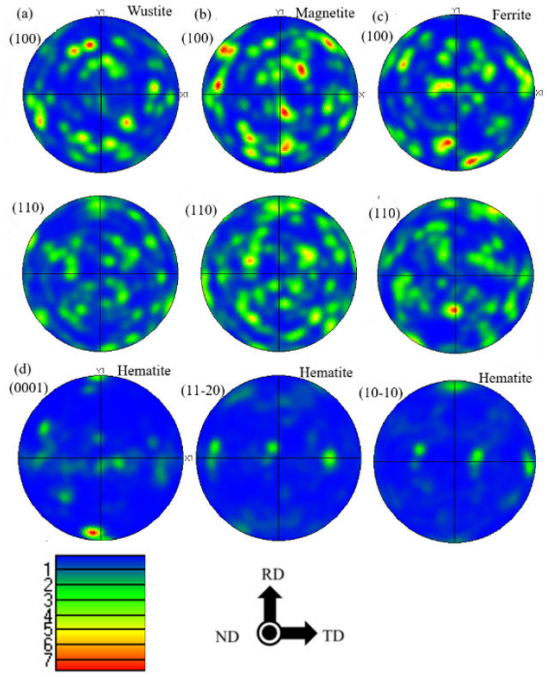


Figure 9. Polar diagrams of the oxide layer and steel matrix on different crystal planes for (**a**) FeO, (**b**) Fe_3O_4, (**c**) ferrite, and (**d**) (0001), (10−10) and (11−20) PF for Fe_2O_3, with a TR of 10%, and a CR of 11 °C/s.

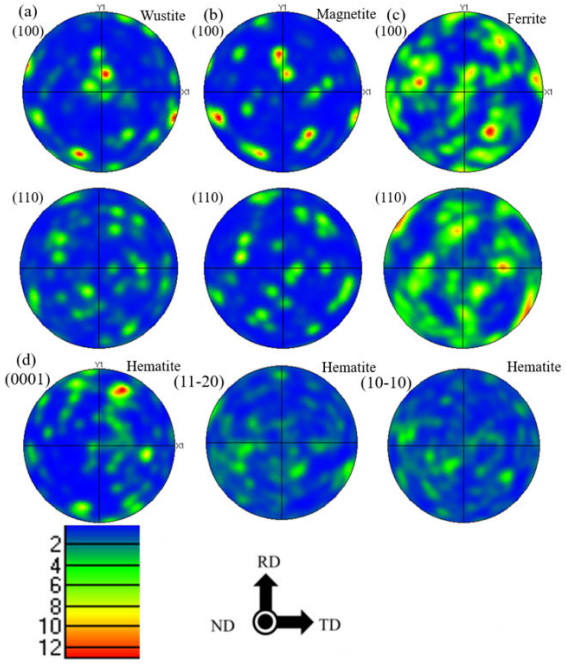


Figure 10. Polar diagrams of oxide layer and steel matrix on different crystal planes for (**a**) FeO, (**b**) Fe_3O_4, (**c**) ferrite, and (**d**) (0001), (10−10) and (11−20) PF for Fe_2O_3, with a TR of 15%, and a CR of 18 °C/s.

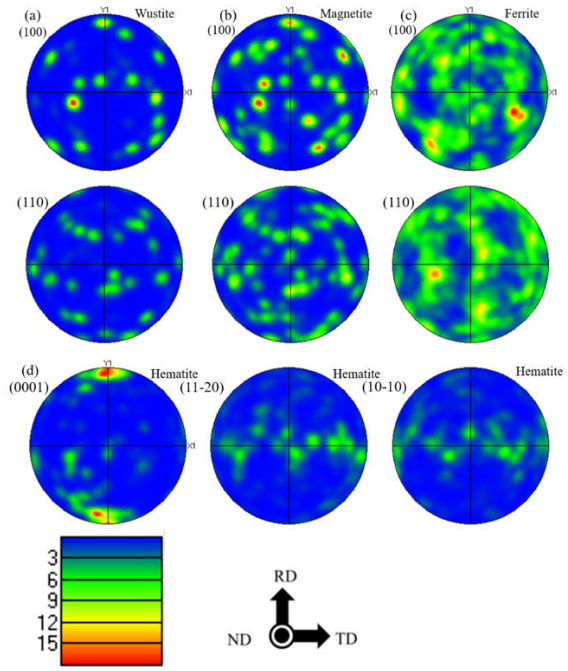


Figure 11. Polar diagrams of an oxide layer and steel matrix on different crystal planes for (**a**) FeO, (**b**) Fe_3O_4, (**c**) ferrite, and (**d**) (0001), (10−10) and (11−20) PF for Fe_2O_3, with a TR of 27%, and a CR of 27 °C/s.

The Schmidt factor is very important for model predictive analysis, mainly because it involves the critical slitting stress of the material, the geometric relationship between the slip system and the force axis. The Schmidt factor is also called the orientation factor, and its analysis is based on the slip system in the crystal, which is based on the energy consumption of the specified crystal shape. According to the tensile deformation mechanism and critical deformation of metal single crystal, i.e., the force law, the yield strength has the following relationship:

$$\sigma_{0.2} = \frac{\tau}{(\cos\varphi * \cos\lambda)_{max}} \quad (1)$$

where τ represents the critical resolved shear stress, determined by the nature of the sheet material, φ is the angle between the force axis and the normal of the sliding surface, λ represents the angle between the force axis and the slip direction.(cosφ*cosλ) is called the Schmid factor, denoted as m_s.

We can therefore calculate the Schmidt factor based on the texture result obtained after hot rolling.

3.5. The Formation Mechanism of Fe_3O_4 Joint Seam Layer

The changes in the grain orientation of Fe_3O_4 in the oxide scale under different thickness reduction and cooling rates are evaluated by the Schmidt factor. When the reduction rate is 10% and the cooling rate is 11 °C/s, the Schmidt factor in {114}<110> grains direction has the value (η_s = 0.4389). On the contrary, when the reduction rate is 27%, {112}<−1−21> texture component of Fe_3O_4 has the largest Schmidt factor value (η_s = 0.4945). When the reduction rate is 15% and the cooling rate is 18 °C/s, the Schmidt factor falls somewhere in between, and the value is 0.4621. With the increase in the reduction rate, the fiber texture components of <110> and <111> of cubic crystal system materials continuously increase. Under normal, the important slip system of Fe_3O_4 crystal structure at room temperature is {111}<110> and {114}<110> texture, that is to say, it usually produces {110} fiber texture component [20,21]. When the reduction rate is 27%, {112}<−1−21> slip system shows the lowest Schmidt factor value. The results show that during the high-temperature rolling of the steel plate, other textures around the grains are consumed, so that {112}<1−1−2>

texture components can be maintained. The main reason is that this type of texture component is the most effective in resisting local plastic deformation. The development process of {114}<1−10> texture to {112}<−1−21> also reflects the deformation substructure in-grain deformation. When the crystal grains undergo plastic deformation, the high Schmidt factor crystal grains will be plastically deformed earlier than the low Schmidt factor crystal grains, so that the low Schmidt factor crystal grains present higher storage strain energy. That is to say, under the condition of higher reduction rate and sharing of plastic deformation, the lower Schmidt factor grains are more difficult to operate than the high Schmidt factor grains; that is, more strain energy is stored. For Fe_3O_4 grains deformed by high-temperature shaping and rolling, the {112}<−1−21> direction texture will first consume the surrounding grains during the deformation process, which is shaped by storage determined by the strain energy of deformed grains. In addition, the anisotropy of strain energy is proportional to the reduction rate.

Fe_3O_4 and FeO formed at the initial high temperature share the {100} fiber texture, also known as the theta fiber texture [22,23]. This fibrous grain shape is rooted in the Fe_3O_4 seam layer between the oxide layer and the matrix. This result indicates that the strain lateral growth process exists in the high-temperature oxidation process. After the hot rolling, the stress release appears at the interface, that is to say, there is almost no strain at the interface. The Fe_3O_4 grains formed by the phase transformation are generated by nucleation, and the grains grow by diffusion [24–26]. The preferential orientation growth of the oxide layer grains reflects the energy balance between the internal stress state [27] of the oxide layer and the ion transport in the steel matrix [28]. In this experiment, the oxide scale is mainly composed of outer granular grains, middle columnar grains, and spherical Fe_3O_4 grains near the substrate [29–31]. The formation of the equiaxed crystals of this fine grain is closely related to the preferred orientation of the oxide layer. It also involves the diffusion of ion vacancies in the oxide layer. The specific internal stress state caused by these phenomena causes the inner oxide scale. The stress state changes are shown in Figure 12 below.

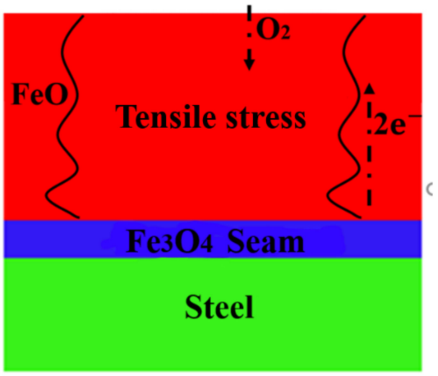


Figure 12. Schematic diagram of the stress state of the interface between the oxide layer and the matrix.

For the two-phase isomerized Fe_3O_4 seam layer, when the rolling reduction rate is low, the fiber texture of <110> appears along the growth direction of the oxide layer. This kind of spherical grains preferentially nucleates and precipitates Fe_3O_4 at the Fe surface grains <110>, which can minimize the mismatch behavior between the steel matrix and the oxide Fe_3O_4 lattice. The high-strength steel matrix grains help to increase the deformation between Fe_3O_4 and the matrix, this deformation will lead to the release of stress and even lead to slight tensile stress [32] in the Fe_3O_4 layer at the interface [33].

The ion transport process is shown in Figure 13. The tensile stress in the oxide layer at the interface inhibits the outward diffusion of cations in the oxide scale, and at the same time, the diffusion of oxygen and anions is enhanced. Oxygen anion radius is about 1.4 Å, and $Fe_{(II)}$ and $Fe_{(III)}$ ions' radii are 0.74 Å and 0.64 Å, respectively. The radius of iron cations is about half of that of the oxygen anion. Due to the difference in size, the oxygen anion

in Fe_3O_4 tends to form a cubic structure, in which iron ions occupy part of the octahedral space. Since the radius of iron cations is close to that of alloying elements, when the vacancy concentration is lower than the critical concentration, the generated oxygen ion vacancies form crystal defects. This oxidation process is greatly affected by oxygen vacancies because oxygen vacancies promote the diffusion of oxygen anions.

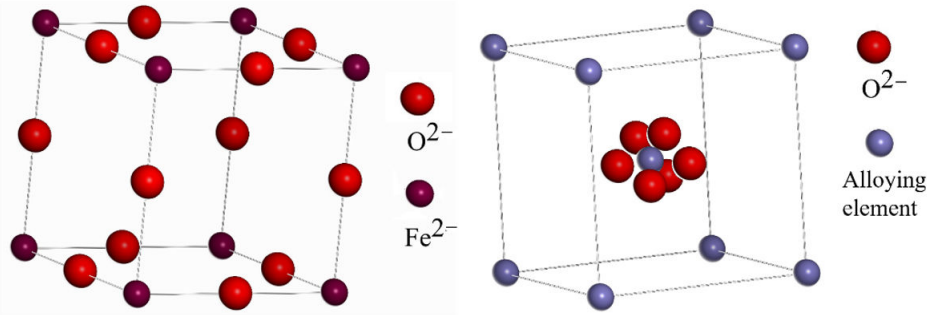


Figure 13. Schematic diagram of ion transmission at the interface between oxide layer and matrix.

4. Conclusions

In the present research, the texture evolution of the oxide scale under different rolling processes and cooling rates was studied through the EBSD analysis method and the sample processing method combining mechanical and argon ion polishing. The results are as follows:

(1) The Fe_3O_4 phase in the oxide layer has a two-phase heterogeneous morphology, Fe_3O_4 in the oxide layer comprises columnar grains, and Fe_3O_4 near the substrate comprises spherical grains. Fe_2O_3 is gradually wedged in the surface of the Fe_3O_4 layer when the rolling reduction rate is low.

(2) Fe_3O_4 and FeO formed at the initial high temperature share a {100} fiber texture. Fe_3O_4 forms a <110> fiber texture at a reduction rate of 10%. The inner layer of the oxide scale is spherical grains, Fe_3O_4 is preferentially nucleated and precipitated in the direction of Fe surface grains <110>, which can minimize the mismatch behavior between the steel matrix and the oxide Fe_3O_4 lattice. With the increasing of the reduction rate, the {112}<−1−21> directional slip system shows the lowest Schmidt factor value, that is, when the crystal grain is deformed, the grains with a higher Schmid factor undergo plastic deformation before the grains with a low Schmidt factor, so the grains with a low Schmidt factor will exhibit higher stored strain energy.

(3) The formation of the preferred orientation of the Fe_3O_4 spherical seam layer is the result of the joint effect of the stress state near the substrate and ion diffusion. The control of grain boundary engineering can provide a certain theoretical basis for pickling-free steel.

Author Contributions: Conceptualization, H.W.; methodology, Z.L.; software, L.L.; validation, P.Z.; writing—original draft preparation, C.W.; writing—review and editing, C.W. All authors have read and agreed to the published version of the manuscript.

Funding: This research was funded by Major Science and Technology Program for Water Pollution Control and Treatment, grant number 2017ZX07402001.

Data Availability Statement: Not available.

Acknowledgments: I would like to show my deepest gratitude to my supervisor, Huibin Wu, a respectable, responsible and resourceful scholar, who has provided me with valuable guidance in every stage of the writing of this thesis. Without his enlightening instruction, impressive kindness and patience, I could not have completed my thesis. His keen and vigorous academic observation enlightens me not only in this thesis but also in my future study.

Conflicts of Interest: The authors declare no conflict of interest.

References

1. Yuan, Q.; Xu, G.; Zhou, M.; He, B.; Hu, H. The effect of P on the microstructure and melting temperature of Fe2SO4 in silicon-containing steels investigated by in situ observation. *Metals* **2017**, *7*, 37. [CrossRef]
2. Li, Z.F.; Cao, G.M.; Lin, F.; Cui, C.Y.; Wang, H.; Liu, Z.Y. Phase transformation behavior of oxide scale on plain carbon steel containing 0.4wt.%CR during continuous cooling. *ISIJ Int.* **2018**, *58*, 2338–2347. [CrossRef]
3. Abuluwefa, H.; Guthrie, R.I.L.; Ajersch, F. The effect of oxygen concentration on the oxidation of low-carbon steel in the temperature range 1000 to 1250 °C. *Oxid. Met.* **1996**, *46*, 423–440. [CrossRef]
4. Chen, R.Y.; Yuen, W.Y.D. Review of the high-temperature oxidation of iron and carbon steels in air or oxygen. *Oxid. Met.* **2003**, *59*, 433–468. [CrossRef]
5. Zhou, C.H.; Ma, H.T.; Li, Y.; Wang, L. Eutectoid magnetite in wüstite under conditions of compressive stress and cooling. *Oxid. Met.* **2012**, *78*, 145–152. [CrossRef]
6. Gleeson, B.; Hadavi, S.; Young, D.J. Isothermal transformation behavior of thermally-grown wüstite. *Mater. High Temp.* **2000**, *17*, 311–319. [CrossRef]
7. Hayashi, S.; Mizumoto, K.; Yoneda, S.; Kondo, Y.; Tanei, H.; Ukai, S. The mechanism of phase transformation in thermally-grown FeO scale formed on pure-Fe in air. *Oxid. Met.* **2013**, *81*, 357–371. [CrossRef]
8. Kim, B.-K.; Szpunar, J. Orientation imaging microscopy for the study on high temperature oxidation. *Scr. Mater.* **2001**, *44*, 2605–2610. [CrossRef]
9. Reichel, F.; Jeurgens, L.P.H.; Mittemeijer, E. The effect of substrate orientation on the kinetics of ultra-thin oxide-film growth on Al single crystals. *Acta Mater.* **2008**, *56*, 2897–2907. [CrossRef]
10. Juricic, C.; Pinto, H.; Cardinali, D.; Klaus, M.; Genzel, C.; Pyzalla, A.R. Effect of substrate grain size on the growth, texture and internal stresses of iron oxide scales forming at 450 °C. *Oxid. Met.* **2012**, *73*, 15–41. [CrossRef]
11. Evans, A.; Hutchinson, J. The thermomechanical integrity of thin films and multilayers. *Acta Met. Mater.* **1995**, *43*, 2507–2530. [CrossRef]
12. Hu, J.; Du, L.X.; Wang, J.J.; Sun, Q.Y. Cooling process and mechanical properties design of hot-rolled low carbon high strength microalloyed steel for automotive wheel usage. *Mater. Des.* **2014**, *53*, 332–337. [CrossRef]
13. Suárez, L.; Rodríguez-Calvillo, P.; Houbaert, Y.; Colás, R. Oxidation of ultra low carbon and silicon bearing steels. *Corros. Sci.* **2010**, *52*, 2044–2049. [CrossRef]
14. Suárez, L.; Rodríguez-Calvillo, P.; Houbaert, Y.; Garza-Montes-de-Oca, N.F.; Colás, R. Analysis of deformed oxide layers grown on steel. *Oxid. Met.* **2011**, *75*, 281–295. [CrossRef]
15. Jia, T.; Liu, Z.; Hu, H.; Wang, G. The optimal design for the production of hot rolled strip with "tight oxide scale" by using multi-objective optimization. *ISIJ Int.* **2011**, *51*, 1468–1473. [CrossRef]
16. Arndt, M.; Duchoslav, J.; Steinberger, R.; Hesser, G.; Commenda, C.; Samek, L.; Arenholz, E.; Stifter, D. Nanoscale analysis of the influence of pre-oxidation on oxide formation and wetting behavior of hot-dip galvanized high strength steel. *Corros. Sci.* **2015**, *93*, 148–158. [CrossRef]
17. Lehockey, E.M.; Palumbo, G.; Lin, P. Grain boundary structure effects on cold work embrittlement of microalloyed steel. *Scripta Mater.* **1998**, *39*, 353–358. [CrossRef]
18. Tanei, H.; Kondo, Y. Effects of initial scale structure on transformation behavior of wüstite. *ISIJ Int.* **2012**, *52*, 105–109. [CrossRef]
19. Chen, R.Y.; Yuen, W.Y.D. Short-time oxidation behavior of low-carbon, low-silicon steel in air at 850–1180 °C-III: Mixed linear-and-parabolic to parabolic transition determined using local mass-transport theories. *Oxid. Met.* **2010**, *74*, 255–274. [CrossRef]
20. Wenk, H.; Canova, G.; Molinari, A.; Mecking, H. Texture development in halite: Comparison of Taylor model and self-consistent theory. *Acta Met.* **1989**, *37*, 2017–2029. [CrossRef]
21. Till, J.L.; Moskowitz, B. Magnetite deformation mechanism maps for better prediction of strain partitioning. *Geophys. Res. Lett.* **2013**, *40*, 697–702. [CrossRef]
22. Birosca, S.; Higgingson, R.L. Phase identification of oxide scale on low carbon steel. *Mater. High Temp. Technol.* **2005**, *22*, 179–184. [CrossRef]
23. Fedorova, E.; Monceau, D.; Oquab, D. Quantification of growth kinetics and adherence of oxide scales formed on Ni-based superalloys at high temperature. *Corros. Sci.* **2010**, *52*, 3932–3942. [CrossRef]
24. Yu, X.; Jiang, Z.; Zhao, J.; Wei, D.; Zhou, C.; Huang, Q. Crystallographic texture based analysis of Fe_3O_4/α-Fe_2O_3 scale formed on a hot-rolled microalloyed steel. *Trans. Iron Steel Inst.* **2015**, *55*, 278–284. [CrossRef]
25. Zhao, J.; Lee, J.H.; Kim, Y.W.; Jiang, Z.; Lee, C.S. Enhancing mechanical properties of a low-carbon microalloyed cast steel by controlled heat treatment. *Mater. Sci. Eng. A.* **2013**, *559*, 427–435. [CrossRef]
26. Ubhi, H.S.; Brough, I.; Larsen, K. Study of recovery and recrystallisation in a folded Al alloy. *Mater. Sci. Forum* **2013**, *753*, 7–10. [CrossRef]
27. Sun, L.; Muszka, K.; Wynne, B.P.; Palmiere, E.J. Influence of strain history and cooling rate on the austenite decomposition behavior and phase transformation products in a microalloyed steel. *Metall. Mater. Trans. A* **2014**, *45*, 3619–3630. [CrossRef]
28. Li, F.; Sun, Z.; Luo, S.; Fan, L.-S. Ionic diffusion in the oxidation of iron—effect of support and its implications to chemical looping applications. *Energy Environ. Sci.* **2011**, *4*, 876–880. [CrossRef]
29. Yu, X.L.; Jiang, Z.Y.; Yang, D.J.; Bin Wei, D.; Yang, Q. Precipitation behavior of magnetite in oxide scale during cooling of microalloyed low carbon steel. *Adv. Mater. Res.* **2012**, *572*, 249–254. [CrossRef]

30. Wei, D.; Jiang, Z.; Han, J.T. Modelling of the evolution of crack of nanoscale in iron. *Computat. Mater. Sci.* **2013**, *69*, 270–277. [CrossRef]
31. Evans, H.; Li, H.; Bowen, P. A mechanism for stress-aided grain boundary oxidation ahead of cracks. *Scripta Mater.* **2013**, *69*, 179–182. [CrossRef]
32. Veal, B.W.; Paulikas, A.P. Growth strains and creep in thermally grown alumina: Oxide growth mechanisms. *J. Appl. Phys.* **2008**, *104*, 93525. [CrossRef]
33. Veal, B.W.; Paulikas, A.P.; Hou, P.Y. Tensile stress and creep in thermally grown oxide. *Nat. Mater.* **2006**, *5*, 349–351. [CrossRef]